Effects of Sn Doping on the Manufacturing, Performance and Carbon Deposition of Ni/ScSZ Cells in Solid Oxide Fuel Cells

Arifin, Nor Anisa; Troskialina, Lina; Shamsuddin, Abd Halim; Steinberger-Wilckens, Robert

Accepted by IJHE, 14 July 2020, manuscript no. HE_HE-D-20-03076

Effects of Sn Doping on the Manufacturing, Performance and Carbon Deposition of Ni/ScSZ Cells in Solid Oxide Fuel Cells

Nor Anisa Arifin[1,2*], *Lina Troskialina*[1,3], *Abd Halim Shamsuddin*[2] *and Robert Steinberger-Wilckens*[1]

[1]Centre of Fuel Cell and Hydrogen Research, University of Birmingham, B15 2TT, United Kingdom

[2]Institute of Sustainable Energy, Universiti Tenaga Nasional, 43000 Kajang, Selangor, Malaysia

[3]Chemical Engineering Department, Politeknik Negeri Bandung, Bandung, 40012 Jawa Barat, Indonesia

[*] Corresponding author: anisa.arifin@uniten.edu.my

Abstract

This work demonstrates the effect of tin (Sn) doping on the manufacturing, electrochemical performance, and carbon deposition in dry biogas-fuelled solid oxide fuel cells (SOFCs). Sn doping via blending in technique alters the rheology of tape casting slurry and increases the Ni/ScSZ anode porosity. In contrast to the undoped Ni/ScSZ cells, where open-circuit voltage (OCV) drops in biogas, Sn–Ni/ScSZ SOFC OCV increases by 3%. The maximum power densities in biogas are 0.116, 0.211, 0.263, and 0.314 W/cm^2 for undoped Ni/ScSZ, undoped Ni/ScSZ with 3wt% pore former, Sn–Ni/ScSZ and Sn–NiScSZ with 1wt% pore former, respectively. Sn–Ni/ScSZ reduces the effect of the drop in the maximum power densities by 26% to 36% with the fuel switch. A 1.28 to 2.24-fold higher amount of carbon is detected on the Sn–Ni/ScSZ samples despite the better electrochemical performance, which may reflect an enhanced methane decomposition reaction.

1 Introduction

Solid oxide fuel cells (SOFC) are efficient high-temperature fuel cells with ceramic electrolyte that operate between 600°C and 1000°C[1]. Coupled with combined heat and power system (CHP), the SOFC efficiency can reach up to 90%[2,3]. The key distinction between SOFCs and low-temperature fuel cells is that aside from pure hydrogen the former can operate with alternative fuels, including bio-hythane[4,5], ethanol[6–8], kerosene[9], propane [10–12], ammonia[13,14], syngas[15], methane[16–20], and biogas[14,21–26], where CO also serves as a reactant in the electrochemical reactions[14,19,27–29]. This ability is a remarkable advantage given the high cost of pure hydrogen required in low-temperature fuel cells although when hydrogen produced from renewable energy [30,31]. Furthermore, methane (natural gas) distribution infrastructure already exists whereas the hydrogen distribution network will need to be built from scratch.

Biogas from wastewater treatment plant contains 60 to 80% CH_4, 30 to 50% CO_2, and traces of impurities [32,33]. Biogas utilisation as an alternative fuel is significant, as based on 2012 data, the global biogas production exceeded 56 billion m^3/year with the energy potential of 1212 PJ [34] led by European countries. Pairing this abundant and under-utilized fuel with SOFC with higher efficiency would increase the generated electricity while considerably reducing the carbon footprint of energy services. In addition, studies by Johnson et al.[35] and Hagen et al.[36] show that the presence of CO_2 (instead of pure methane) in biogas can suppress the effect of sulphur poisoning.

The conventional strategy for using hydrocarbon fuels is by implementing a separate (external) reforming chamber [37], which induces additional capital and operating costs, and additional effort for supplying the heat to the reforming reactor. The SOFC module is then fed with

hydrogen or syn-gas from the reforming chamber to avoid the deteriorating effect of carbon deposition on the SOFC anode[37,38]. On the hand, integrating the reforming reaction into the fuel cell itself (internal reforming) allows for internal heat recycling and thus higher efficiency, but also increases the danger of carbon deposition due to the varying conditions and chemical composition of the fuel gas along the flow path through the fuel cell.

For a SOFC fuelled by hydrogen, only the electrochemical conversion to electricity and heat, with the reaction product water occurs (Eq.1)[14]. For carbon fuelled-SOFC with internal reforming, more chemical and electrochemical reactions may occur due to the existence of six species (CH_4, H_2, CO_2, CO, H_2, and C) in the anode side from the feed and the product of different reactions[19,22]. The steam and dry reforming reactions occur internally (Eq. 2a and b, respectively) with hydrogen (H_2) and carbon monoxide (CO) as the products [14,19,22]. Steam reforming reaction (Eq. 2a) may take place even without steam addition on the anode surface from the product of H_2 electrochemical reaction (Eq.1) [14,19]. The dry reforming reaction (Eq. 2b) is an overall reaction of two other major reactions: high temperature methane decomposition (Eq. 3) and carbon oxidation by CO_2 (Eq. 4) [19,22]. Methane decomposition (Eq.3) can occur on both anode substrate (AS) and at the anode functional layer (AFL) [19]. From inspection of Eq.3 and Eq.4, it is clear that both part-reactions need to be in balance since a lack of carbon oxidation according to Eq.4 would otherwise lead to excess carbon remaining on the catalyst surface, essentially forming a soot cover that will deactivate the catalyst on anode[39]. At SOFC operating temperature, water–gas shift reaction (Eq. 6) (or the reverse reaction) may also accompany the reforming reaction [14,22]. The electrochemical reaction (Eqs. 1 and 7) tend to occur at the anode functional layer (AFL) region, where more triple-phase boundary (TPB) areas are found.

$$H_2 + {}^1/_2\, O_2 \rightarrow H_2O \quad (1)$$

$$CH_4 + H_2O \leftrightharpoons 3H_2 + CO \quad (2a)$$

$$CH_4 + CO_2 \leftrightharpoons 2H_2 + 2CO \quad (2b)$$

$$CH_4 \leftrightharpoons C\,(s) + 2H_2 \quad (3)$$

$$C + CO_2 \leftrightharpoons 2CO \quad (4)$$

$$C + H_2O \leftrightharpoons CO + H_2 \quad (5)$$

$$CO + H_2O \leftrightharpoons CO_2 + H_2 \quad (6)$$

$$CO + {}^1/_2\, O_2 \rightarrow CO_2 \quad (7)$$

Deposited carbon can be removed with carbon oxidation with CO_2 (Eq. 4) or steam (Eq.5), which will occur via a sufficient supply of the oxygen sources from steam reforming (Eq. 2a), dry reforming (Eq. 2b). Sumi et al.[40,41] and Farrell et al.[8] shows that significantly less carbon in the area within closer proximity to the electrolyte layer, i.e higher carbon oxidation reaction occurred in the TPB area than that on the further position. Hence, it shows that the oxygen ions that diffuse through the electrolyte in fuel cell operation can also be utilised. SOFC are therefore more prone to carbon formation when idling at open circuit voltage (OCV).

With conventional SOFC cells, the Ni/YSZ anode performance drastically drops when the system is switched from hydrogen to pure methane or biogas fuels expected due to carbon deposition[24,27,42,43]. Carbon deposition may block the TPB and pores on the anode, leads to total anode deactivation, and further halt the SOFC operation[18]. As carbon oxidation also depends on the catalytic activity of the anode material, extensive work focuses on improving the anode catalytic activity for carbon oxidation.

Although Ni is an excellent catalyst for both electrochemical oxidation reaction and reforming reaction in producing hydrogen and syngas (H_2 and CO)[44–48], Ni also prone to carbon deposition. Hence, Ni-free anode with alternative metal[6,17,49] and perovskites material [50,51] that show better tolerance towards carbon are widely investigated. Still, Ni is widely preferred as the metal catalyst in SOFC anode due to poor catalytic activity in the electrochemical reaction, incompatibility with thermal expansion of other SOFC layers, and low mechanical strength of the alternative materials when compared to Ni[22].

Another strategy, avoiding the replacement of Ni, is by reducing the affinity of Ni to carbon by replacing the support oxides (YSZ) or by alloying with other metals[39]. Replacing yttria-stabilized zirconia (YSZ) with scandia-stabilized zirconia (ScSZ) or gadolinia-doped ceria (GDC) can successfully improve the tolerance of the anode when tested in methane and biogas [40,52,53] due to higher availability of oxygen ions for carbon oxidation. ScSZ with higher conductivity than YSZ displays different types of carbon[40,43] and carbon deposition behaviour[40,54,55] compared with Ni/YSZ cells, which is due to the difference in crystalline structure [40,43].

Surface alloying with precious metal such as Pt, Pd, Au, Ru, and Rh[56,57], or base metals, such as Sn, Sm, Co, Fe, Cu, and Ag[24,58,59] can modify Ni in such a way that it preferentially oxidizes C atoms to CO and CO_2 rather than forming C–C bonds[58]. Jiang et al.[24] showed that alloying Ni with Sn achieves the best performance compared with Ag and Cu. Across several works, the electrochemical performance of Sn–Ni/YSZ cells is unchanged or within 5% of drop when the fuel is switched from hydrogen to methane or dry biogas, whereas that of Ni/YSZ cells substantially drops[18,27,60].

Using density functional theory and temperature-programmed reduction with humidified hydrocarbon fuels on Sn–Ni/YSZ, Nikolla et al. [58] suggested that (i) Sn/Ni catalyst has higher efficiency in forming C-O bonds than C-C bonds compared to Ni, which resulted in less solid carbon deposited on the anode, (ii) Higher active sites of Sn/Ni compared to under-coordinated Ni active sites, and (iii) Sn/Ni lessen the binding strength of carbon atoms on the anode. In agreement with studies by Nikolla et al.[58], Kan et al.[18] and Farrel et al.[8] shows less amount of carbon detected on most of the Sn doped cells with humidified fuel or high oxygen to carbon ratio fuel. Kan et al.[18] shows improved stability with operation up to 137 hours with Sn-Ni/YSZ cell compared to 27 hours with undoped cells in humidified methane. On the other hand, Singh et al. [42] and Lay et al. [61] reported no significant performance difference and higher amounts of carbon observed on the Sn doped cells compared to the undoped cells with either low steam to carbon ratio. Troskialina et al.[27] and Jiang et al.[60] tested Sn-Ni/YSZ with dry biogas fuel instead of humidified hydrocarbon fuel. All studies [8,27,42] agreed on small amount of Sn (1wt%) as the optimum quantity, in which a higher concentration of Sn decreases the performance due to an increase in polarisation resistance.

To date, the effect of Sn/Ni alloying has only been tested on Ni/YSZ cells mostly via the surface impregnation method. The metal surface impregnation method introduces several additional steps where the catalyst needs to be repeatedly dispersed on the targeted surface followed by drying and calcination to remove the precursor [27,42]. The work reported here attempted to i) investigate the impact of Sn doping on the electrochemical performance of biogas internal reforming on Ni/ScSZ and the amount of carbon deposited, and ii) test alternative and simpler dopant introduction methods by blending in with the tape casting slurry.

2 Experimental

2.1 Materials

The as-received commercial powders used for electrolytes were 10ScCeSZ ($(Sc_2O_3)_{0.1}$–$(CeO_2)_{0.01}$–$(ZrO_2)_{0.89}$); from DKKK with an average particle size of 0.514 ± 0.053 μm (d_{50}). For the anode substrate (AS), coarse nickel oxide (NiO) with a particle size of 8.101 ± 0.185 μm (d_{50}) from Novamet and pre-calcined 10ScCeSZ (DKKK) with a particle size of 0.372 ± 0.001 (d_{50}) were used with a weight ratio of 65:35. Fine as-received NiO (Pi-Kem Ltd.) with an average particle size of 0.637 ± 0.145 μm and as-received 10ScCeSZ (DKKK) were mixed in the same ratio for the anode functional layer (AFL). $SnCl.2H_2O$ (Sigma Aldrich, UK) was used as the precursor of Sn to produce Sn-doped Ni/ScSZ cells. As-received lanthanum strontium manganese, $La_{0.80}Sr_{0.20}MnO_3$ (LSM, Praxair) with an average particle size of 0.90 μm was used for cathode.

2.2 Methodology

2.2.1 Sn–Ni/Scsz Cell Fabrication Via Aqueous Tape Casting

Figure 1 shows the two ball-milling mixing steps performed for the full-cell fabrication of the standard Ni/ScSZ cells, as reported in previous work [53]. For Sn-doped cells, $SnCl_2.H_2O$ (1wt% of Sn/Ni) was pre-dispersed with NiO powder by ball milling for 1 h at 120 rpm with water and dispersant. Then, 0wt% and 1wt% pore former were used in this Sn–NiScSZ formulation in accordance with the practicality of the manufacturing method and the targeted porosity of the cells. A high amount of plasticizer and binder was used in leverage to the pore former amount for cells with less pore former, and the 1:1 ratio of binder to plasticizer and solid loading of 55 wt% was maintained. The same formulation with 0wt% and 3wt% pore former was used for undoped Ni/ScSZ cells. The porosity of the reduced anode shown in Table 2 was measured via the Archimedes method.

A reverse or co-casting tape-casting method [53,62,63], with inverted layer application to the conventional method was used with an aqueous-based formulation. A thin layer of electrolyte was cast first, followed by AFL and AS with drying periods in between. Tape casting was carried out with a laboratory scale tape-casting machine (L800 by MTI) on a silicone-coated PET film. Drying was performed in a low-temperature oven with no air blown to avoid cracks. Table 1 shows the settings applied for tape casting. The button cells with 3 cm diameter produced were co-sintered at 1280°C for 4 h with 1°C/min heating rate and an organic burnout stage at 550°C. 10 g of dead-weight was used to ensure the cell flatness. During high temperature sintering, Cl in the $SnCl_2.H_2O$ is removed, leaving the oxides form. This has been shown in XRD and XPS analysis in previous work in the same research group[22,60]. The LSM cathode ink was produced using a three-roll mill machine (BUHLER) for mixing the cathode powders with a Haraeus V-737 ink vehicle (22.6 vol% solids). The sintered half-cells were hand-painted with a 15 µm thick LSM layer with an effective area of 2 cm^2 and sintered again at 1100°C.

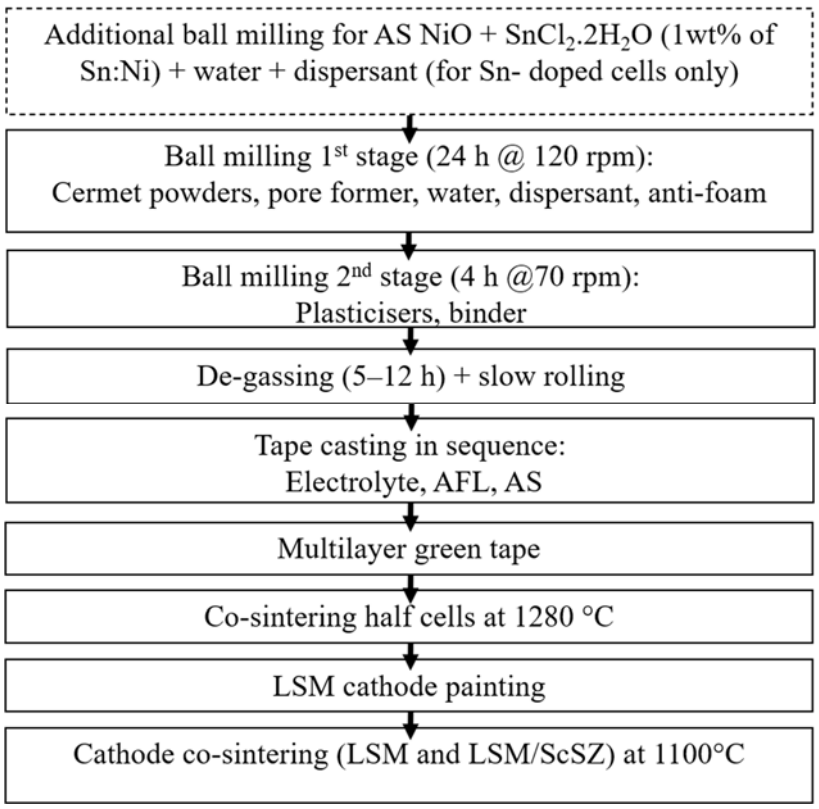

Figure 1. SOFC full-cell manufacturing.

Table 1: Tape-casting setting for different layers.

	Electrolyte	**AFL**	**AS**
Speed (mm/s)	3.33	6.33	6.33
Gap (µm)	10–12	15	200
Drying temperature/time	70 °C/10 to 15 min	70 °C/10 to 15 min	33 °C/Overnight

Table 2. Description of fabricated in-house cells.

	Description	**Porosity (%)**
USC	NiSc	28.5
USC3P	NiSc with 3wt% pore former	39.8
TSC	Sn–NiSc	31.0
TSC1P	Sn–NiSc with 1wt% pore former	38.5

2.2.2 Electrochemical Performance

The testing setup was similar to the one previously described in [53]. Leakage test carried out with He at 750°C prior to feeding with hydrogen. The cells were characterized for 24 h at 750°C in hydrogen by using 21 ml/min H_2 and 7 ml/min He, followed by 24 h in dry biogas at a flowrate of 14 ml/min CH_4, 7 ml/min CO_2 and 7 ml/minute He. The comparison was made using the open-circuit voltage (OCV), maximum power densities, and electrochemical impedance spectroscopy (EIS), measured in turns. EIS analysis was performed at 0.7 V within a frequency range of 0.1 Hz to 1M Hz with a signal amplitude of 10 mV.

2.2.3 Post-test Analysis

Microstructural analysis was conducted with a scanning electron microscopy (Hitachi TM3030) with a magnification of 5k and acceleration of 15kV with unpolished and uncoated fragments from tested SOFC cells. Temperature-programmed oxidation (TPO) tests were conducted to quantify the amount of carbon in the SOFC-tested cells. 200gram of SOFC-tested fragments were placed in the middle of a quartz chamber with compressed air flow rate of 50 ml/min for carbon oxidation. The furnace was ramped to 600°C at 5°C/min and annealed for 1 h to allow complete carbon oxidation. The outlet gas tube was connected to a mass spectroscopy machine (MKS-Cirrus, USA) for evaluation. TPO was calibrated using three known amounts of carbon graphite powder (10.1, 1.2 and 0.7 g) prior to the actual sampling. The resulting CO_2 peak areas were used to construct a calibration curve (supplied in supplementary material section). The calibrated value obtained used as a factor to quantity the amount of carbon on the tested cells.

3 Results and discussion

3.1 Effect of Sn Doping on Full-Cell Manufacturing

The addition of $SnCl_2.H_2O$ to the anode substrate slurry in either the first or second stage resulted in a thick slurry, which cracked when completely dried (Figure 2). The mud-cracked tape in Figure 2 originated from the uneven drying or drying gradient between the bulk of the slurry and the skin of the tape. Blend-in doping with the tape-casting slurry was achieved by introducing an additional premixing described in the methodology section. Mixing via ball milling with only NiO powder increased the probability of Sn adherence to the Ni surface rather than the ScSZ. The microstructural analysis of the sintered full cell (Figure 3a) revealed the microstructure of TSC (Sn–Ni/ScSZ cells) with dense electrolyte and porous anode substrate. Figure 3c shows the anode substrate of TSC after NiO reduction, which created a more porous structure compared with the anode substrate before reduction (Figure 3b). The average anode porosity of TSC was 31.0%, which was higher than that of undoped cells (USC) (28.5%), although the same setting was used. TSC1P (Sn–Ni/ScSZ with 1wt% pore former) and USC3P (undoped Ni/ScSZ with 3wt% pore former) were fabricated with a final porosity volume of 38.5% and 39.8%, respectively. With the 55wt% solid loading used, the addition of more than 1wt% pore former in the Sn–Ni/ScSZ formulation resulted in a thick slurry, which limited further addition of pore former. Increased porosity in the anode substrate leads to a decrease in mass diffusion resistance, i.e higher performance, as long as the porosity level still within optimum porosity level (<40%) [64,65]. Hence, due to the influence of Sn addition to porosity, cells with similar porosity levels were targeted and tested.

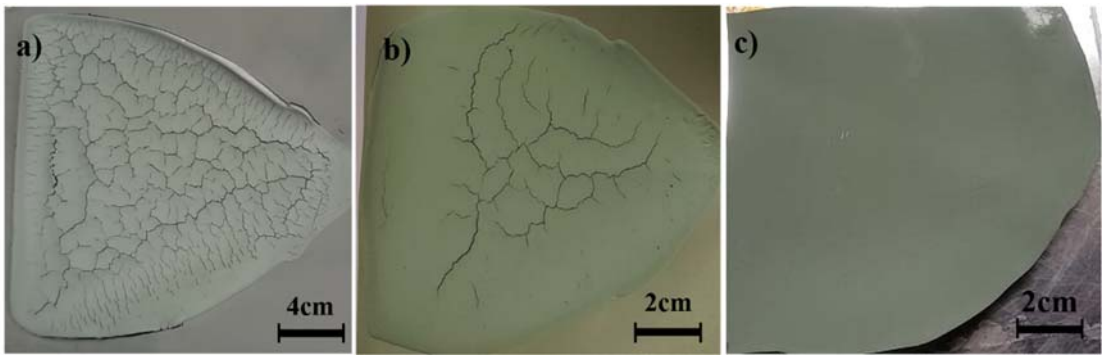

Figure 2. Ni/ScSZ green tape with blend-in $SnCl_2.2H_2O$ with different addition stages; a) after the first ball milling, b) after the second ball milling, and c) additional premixing step with NiO, dispersant and water.

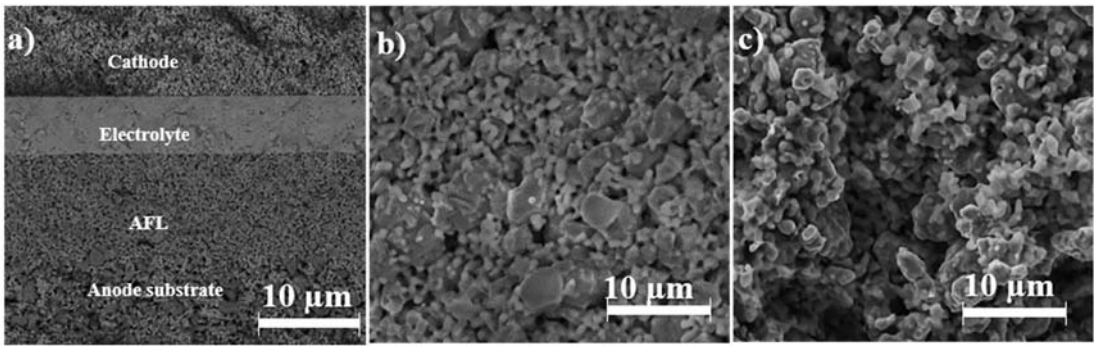

Figure 3. TSC before SOFC cell test, a) cross-section image, b) anode substrate before reduction, and c) anode substrate after reduction.

3.2 Electrochemical performance

3.2.1 Open circuit voltage

Initially in the hydrogen test, the test was run under OCV mode for six hours for complete reduction of the cells while the first run of SOFC in biogas was 90 minutes in OCV mode to minimise carbon deposition. The OCV measured alternately with iV curve, impedance, and potentiostatic. Figure 4a shows that in TSC (Sn–Ni/ScSZ with 0 wt% pore former), the open-circuit voltage (OCV) in hydrogen was stabilized at 1.03 V 80 minutes after hydrogen was introduced and gradually dropped to 1.02 V. With the fuel swap from hydrogen to biogas (BG), the OCV value was higher than that generated in hydrogen (1.05 V). Figure 4b shows the same trend observed in TSC1P (Sn–Ni/ScSZ with 1 wt% pore former), whilst the opposite trend was

observed with the undoped Ni/ScSZ cells (USC and USC3P). OCV also increased in Sn–Ni/YSZ cells reported previously by Troskialina et al. [27].

The Nernst equation for the electrochemical reaction for H_2 (Eq.1) is presented by Eq.8, which in analogy also applies to Eq.7, the CO oxidation. E^0 is the open-circuit voltage (OCV), also called the reversible potential or electromotive force (EMF), can be calculated from the Gibbs free energy for the respective reaction and the Faraday constant as shown in Eq.9. Gibbs free energy of CO oxidation at 750°C is higher than that of H_2 oxidation, which are –191.5 kJ/mol and -193.6 kJ/mol [66], respectively. Substituting these values in Eq.9, the theoretical OCVs at 750°C are 1.03V and 0.99V for H_2 and CO respectively. Higher OCV value from the CO electrochemical oxidation expected to increase the OCV when biogas is used, but the OCV dropped instead in the undoped cells. The difference in OCV value in biogas setup between the Sn doped and undoped cells may reflect the difference in dry methane reforming (Eq.2b) ability, which has higher OCV value as reported by You et al. [19].

$$E = E^0 + \frac{RT}{2F} ln\left(\frac{p_{H_2} {p_{O_2}}^{1/2}}{p_{H_2O}}\right) \quad (8)$$

$$E^0 = -\Delta G^0_{rxn}/2F \quad (9)$$

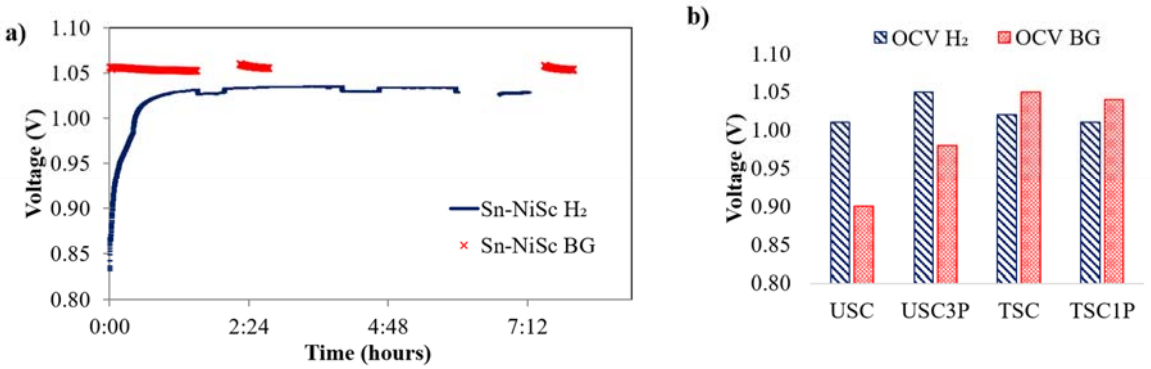

Figure 4. OCV when tested in hydrogen (H_2) and biogas (BG) of a) Sn–Ni/ScSZ SOFC cell (TSC) and b) across different cells, Sn-doped and undoped cells.

3.2.2 Maximum power densities and impedance analysis

Figure 5 shows that the first maximum power densities obtained in hydrogen were 0.252, 0.450, 0.339, and 0.404 W/cm^2 for USC, USC3P, TSC, and TSC1P, respectively. In all cells, the constant degradation observed in the *i*V–PV curve may be due to Ni coarsening in the cermet, which reduces the catalytic surface area in the fuel cell. This well-known initial process in SOFC has also been reported by Farrell et al.[8]. With an average 16% of cell degradation, the maximum power densities in hydrogen before the fuel swap were 0.220, 0.331, 0.297, and 0.349 W/cm^2 for USC, USC3P, TSC, and TSC1P, respectively. US3P observed to have higher degradation in hydrogen (Figure 5) compared to other cells. It is suspected to be due to the high porosity level, which near the maximum recommended limit (40%). Continuous Ni coarsening and agglomeration may push the porosity limit, reduce the TPB volume, hence the catalytic area and affected the effective conductivity[64,65]. The effect of porosity (Table 2) on cell performance (Figure 5) was considerable, and less porous cells experienced high resistance for the fuel to diffuse through the anode substrate (Figure 6). Hence, the slightly lower performance of TSC1P in hydrogen compared with that of USC3P may be due to the porosity level. The maximum power density of the latter was higher than that of the former. Given the influence of Sn dopant to the cell's porosity, surface impregnation on sintered half cells may be a more suitable method due to this limitation.

When the SOFCs were operated with biogas after the 24 hours test in hydrogen, the performance of the cells dropped. Sn-doped cells were less affected and showed an average of 11% drop in performance with the fuel swap, whilst undoped Ni/ScSZ cells exhibited 36% and 47% drop in performance for USC and USC3P, respectively. The maximum power densities in biogas were 0.116, 0.221, 0.263, and 0.314 W/cm^2 for USC, USC3P, TSC, and TSC1P, respectively. In the undoped cells, polarization increased with time in both hydrogen (0.032 Ωcm^2) and biogas (0.14 Ωcm^2). Surprisingly, the increase in biogas polarization in both TSC

and TSC1P between 26 h and 46 h was not substantial (0.030–0.035 Ωcm^2), as shown by the Nyquist plot in Figure 6. No impedance data were obtained for USC due to a spectrometer failure. Kan et al. [18] observed long-term stability with methane with Sn-doped Ni/YSZ cells, but the power density values obtained in methane operation between the undoped Ni/YSZ cells and doped Sn-Ni/YSZ cell were similar. Troskialina et al. [27] observed similar maximum power density under hydrogen and biogas via surface impregnation with pipette doping; the performance did not drop, which was also observed by Farrell et al. [8].

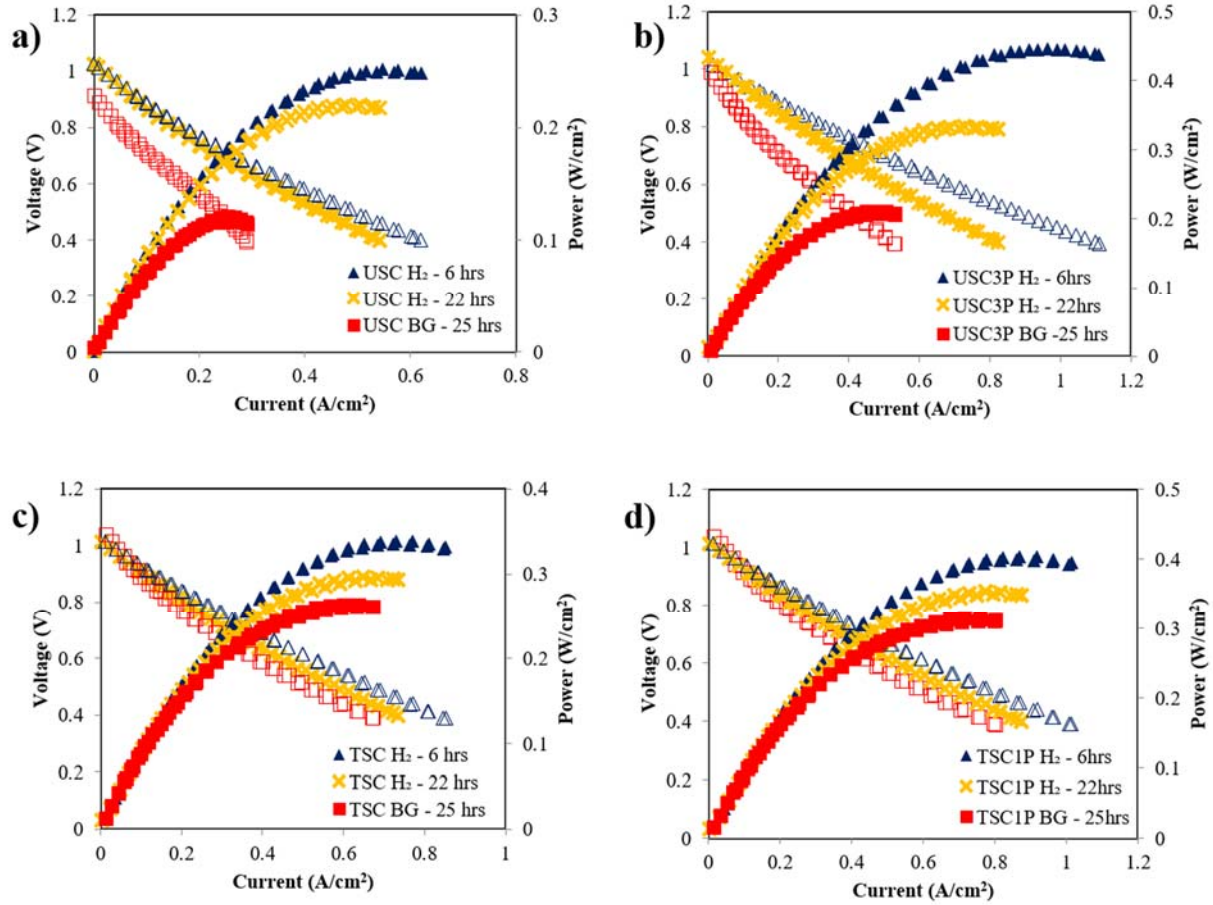

Figure 5. *i*V–PV curve of the cells: a) USC, b) USC3P, c) TSC and d) TSC1P in hydrogen (H_2) and biogas (BG).

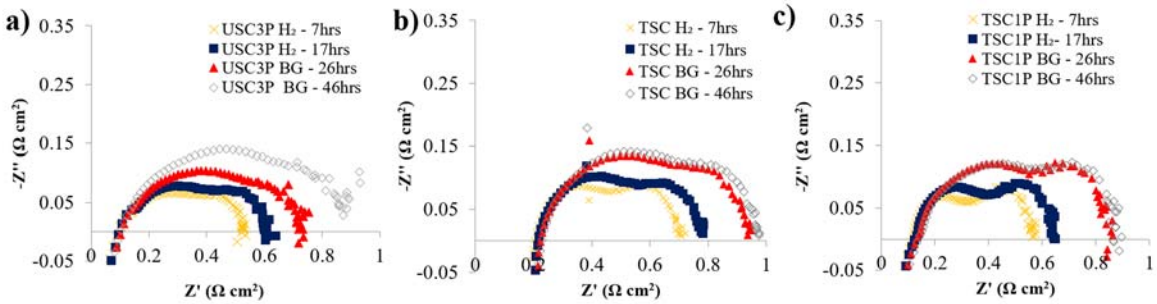

Figure 6. Nyquist plot of a) USC3P, b) TSC, and c) TSC1P and in H_2 and biogas (BG).

3.3 Carbon deposition post-test analysis

3.3.1 SEM microstrucuture analysis

The microstructures of the anode of the undoped sample and Sn-doped cells are shown in Figure 7. In both cases, the filamentous growth structures (circled in red) were visually observed by SEM. Baker et al. [67] explained that filamentous carbon may have a graphitic skin and an amorphous head end. A small amount of graphitic carbon enhances the performance by increasing the Ni anode conductivity via the additional graphitic carbon network [68,69]. Carbon quantification with SEM–energy dispersive X-ray analysis (EDX) is unreliable in this case because the electron signal is affected by the anode's uneven porous structure. Hence, carbon quantification via temperature-programmed oxidation (TPO) was used for evaluating the amount of carbon deposited, corresponding to the amount of CO_2 released.

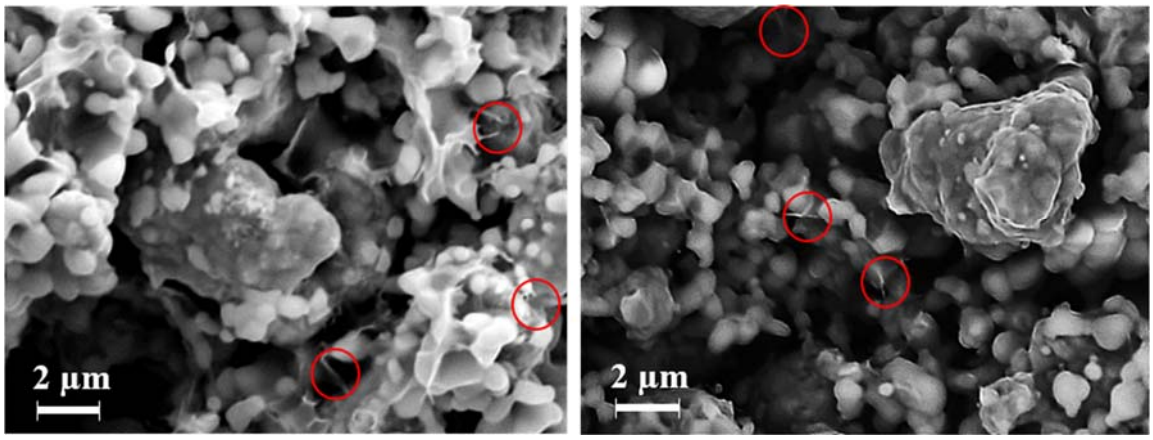

Figure 7. Microstructure of a) USC3P and b) TSC after SOFC cell testing with carbon growth circled in red

3.3.2 Carbon quantification via temperature-programmed oxidation

The graphitic carbon burn-off in this work started at 520°C and completed the combustion at 600°C during the 1-hour dwelling stage (shown in the supplementary material). The CO_2 peaks from the samples observed at 600°C (Figure 8) confirmed that the type of carbon build-up in the samples were graphitic. In USC3P, smaller peaks at 400°C that might originate from amorphous carbon was detected. The amounts of carbon deposited on TSC and TSC1P of Sn–NiScSZ samples were 4.83×10^{-3} and 5.94×10^{-3} mg-C/mg_{cat}, respectively, which were higher than those of undoped Ni/ScSZ cells, USC and USC3P (1.49×10^{-3} and 2.60×10^{-3} mg-C/mg_{cat}). The amount of carbon deposited and the rate of carbon deposition in the samples are presented in Table 3. The carbon deposited and the rate of carbon deposition calculated in this work was the net balance of carbon deposited, subtracting the amount of carbon oxidized to CO_2 and CO during the SOFC electrochemical reaction. The carbon deposition in Ni/ScSZ (40% Ni) anode investigated by Somalu et al. [70] with a quartz tube and with an S/C ratio of 0.8 without electrochemical reaction was 28 mg-C/mg_{cat}.

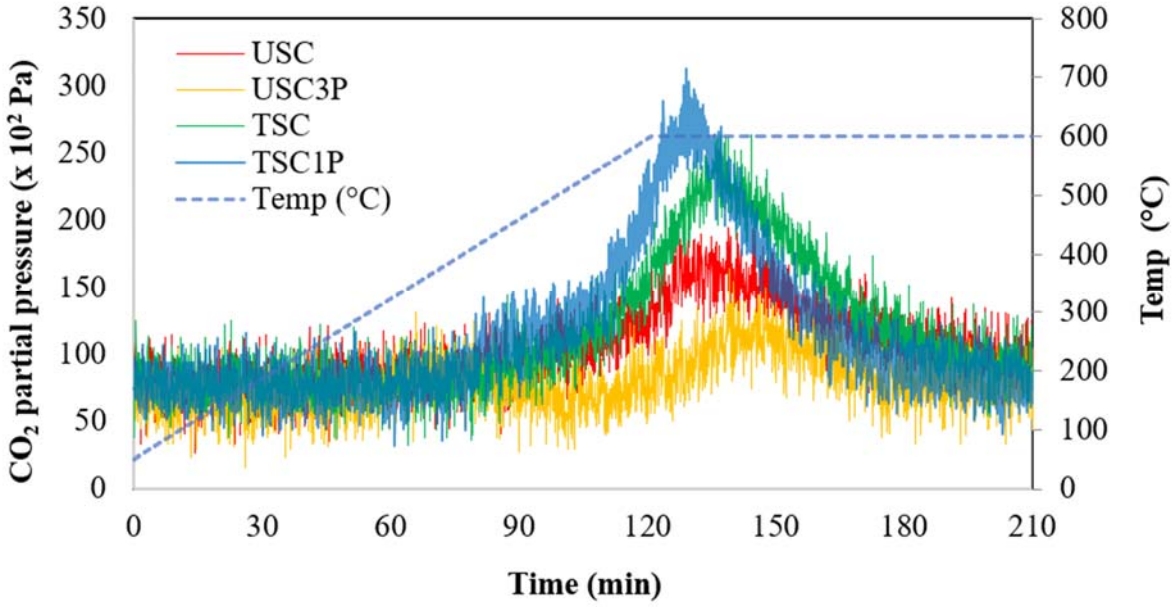

Figure 8. CO_2 peaks from carbon burn off on Sn–Ni/ScSZ and undoped Ni/ScSZ cells.

Table 3. Amount and rate of carbon deposition in undoped and Sn-doped NiScSZ cells.

	Amount of carbon deposited		Rate of carbon deposition (mg-C/g_{cat} h)
	Per sample (mg)	Per unit catalyst (mg-C/mg_{cat})	
USC	0.300	1.49×10^{-3}	0.062
USC3P	0.525	2.60×10^{-3}	0.108
TSC	0.975	4.83×10^{-3}	0.201
TSC1P	1.275	5.94×10^{-3}	0.248

In the present work, although only one burn off temperature that deduced to be graphitic carbon from the burn off temperature (Figure 8), amorphous carbon may also have formed. As amorphous carbon is easier to oxidise, it may have oxidised either from CO_2 (Eq.4), or H_2O (Eq.5), or by oxidation from the electrochemical reaction (Eqs 1 and 6), hence only small amount of amorphous carbon detected in the USC3P in the TPO analysis.

Initially, the improved performance of Sn–NiScSZ suggested that the amount of carbon deposited may be lower than that on the undoped cells due to the assumption that carbon deposition may have hindered the electrochemical reaction. However, the result from TPO showed otherwise. Thus, the decreased performance of undoped Ni/ScSZ cells in the present study was not mainly due to the amount of carbon deposited but inclined to lack of methane decomposition reaction (Eq. 3), hence lowered the amount of H_2. On the other hand, Sn accelerated the activity of the methane decomposition reaction (Eq. 3), thereby releasing an increased amount of H_2 as reactant for the electrochemical reaction and inevitably accompanied by increased amounts of carbon. The result of this present study supported by Troskialina [71]. Troskialina [71] detected a higher amount of carbon in Sn-doped Ni/YSZ cells than in undoped cells, with the carbon peak coinciding with the graphitic carbon burn-off temperature, as observed in the present work.

In the present study, the author speculates that in the region with closer proximity to the electrolyte (i.e the TPB/AFL area), rapid oxidation occurred due to increased electrochemical reactions (Eq. 1) in response to increase amount of H_2. However, in case of carbon deposited in further position (mainly in the anode substrate region), carbon might be oxidised only by CO_2 (Eq. 4) or by H_2O (Eq. 5). In this case, the carbon oxidation by CO_2 (Eq. 4) and by H_2O (Eq. 5) reaction rates might be slower than that of methane decomposition (Eq.3), leading to increased carbon amount in Sn doped cells. Therefore, although small amount of graphitic carbon may still deposit near the TPB electrochemical reaction region, it did not hinder the reaction. On the other hand, it may enhance the electrochemical reaction and electrical conductivity by the extra graphitic network[68,69]. Nonetheless, even with assumption that the TPB area is unaffected, excessive carbon build up in the substrate region must be avoided as it will lead to stress, fracture the support, or push the metal particles off the support[39].

The improve electrochemical performance of Sn doped cells in biogas compared with undoped cells agreed with previous findings[18,27,42]. However, the high amount of carbon formed on the Sn-doped cells in the present study was in contrast to the findings of Farrell et al.[8] and the suggestion of Nikolla et al.[58] on the carbon oxidation ability. The significant difference with this study compared to Nikolla et al.[58] and Farrell et al.[8] is the carbon ratios in the hydrocarbon fuel. In present study, dry biogas is used, while Nikolla et al.[58] conducted the studies with moderate steam to carbon ratio with different fuels and Farrell et al.[8] used ethanol, which has higher oxygen to carbon ratio. On other studies, Singh et al.[42] and Lay et al.[61] reported no significant performance difference and higher amounts of carbon observed on the Sn doped cells compared to the undoped cells with either low steam to carbon ratio or dry methane.

The surface impregnation method showed similar performance in hydrogen and biogas by the Sn-NiYSZ anode when the fuel was switched from hydrogen to humidified methane and biogas [42,71]. Through surface impregnation, almost all dopants adhere to the Ni on the anode substrate surface, which may have better exposure in catalysing the dry reforming reaction as well as increased the electrochemical reaction. On the other hand, doping by the slurry blend-in method practiced in present work may cause the Sn dopant to sit in the cermet bulk and thus not be accessible. Hence, although dopant introduction can be performed easily with slurry blend in method, surface impregnation is more effective. Alternately, relative more dopant would be required, and optimisation need to be carried out to statistically secure sufficient presence on the nickel particle surfaces. Nonetheless, if the main aim of the research is on the influence of Sn as dopant, surface impregnation method is recommended to eliminate the

491 influence of porosity to mass diffusion resistance and conductivity on the electrochemical
492 performance.
493
494 ## 4 Conclusion
495 The electrochemical performance result suggested that Sn doping enhanced the performance
496 of Ni/ScSZ cells in biogas operation, due to improved catalytic activity of the methane
497 decomposition reaction, which is the first step in dry methane reforming reaction. The higher
498 amount of carbon deposited originated from slower carbon oxidation compared to the methane
499 decomposition reaction on Sn-Ni/ScSZ. From the higher amount of carbon affected by the
500 methane decomposition reaction, we found no conclusive evidence on the positive influence
501 of Sn on carbon oxidation on Ni/ScSZ. In further work, a more in-depth understanding on the
502 effect of Sn addition in the dry reforming and carbon oxidation reactions may be possible
503 through prolonged SOFC electrochemical tests and separate reforming catalytic activity tests
504 with Sn–Ni/ScSZ cell with the exhaust gas connected to a gas chromatograph–mass
505 spectrometer. Separate conductivity tests in further work will also assist the understanding of
506 the effect of Sn to anode's porosity and conductivity.
507
508 ## 5 Acknowledgement
509 The results reported herein were based on a Ph.D. work conducted at the Centre of Fuel Cell
510 and Hydrogen Research, University of Birmingham [72]. The authors would like to
511 acknowledge the Council of Trust for the Bumiputera Malaysia (MARA), Human Life
512 Advancement Foundation (HLAF) for funding the Ph.D. work and AAIBE Chair of Renewable
513 Energy Grant No. 201801 KETTHA for funding the publication.
514
515

Reference

[1] Kendall K. Introduction to SOFCs. High-Temperature Solid Oxide Fuel Cells 21st Century Fundam. Des. Appl. Second Ed., Elsevier Inc.; 2016, p. 1–24. https://doi.org/10.1016/B978-0-12-410453-2.00001-4.

[2] Buccheri MA, Singh A, Hill JM. Anode- versus electrolyte-supported Ni-YSZ/YSZ/Pt SOFCs: Effect of cell design on OCV, performance and carbon formation for the direct utilization of dry methane. J Power Sources 2011;196:968–76. https://doi.org/10.1016/j.jpowsour.2010.08.073.

[3] Wang X, Lv X, Weng Y. Performance analysis of a biogas-fueled SOFC/GT hybrid system integrated with anode-combustor exhaust gas recirculation loops. Energy 2020;197. https://doi.org/10.1016/j.energy.2020.117213.

[4] Veluswamy GK, Laycock CJ, Shah K, Ball AS, Guwy AJ, Dinsdale RM. Biohythane as an energy feedstock for solid oxide fuel cells. Int J Hydrogen Energy 2019;44:27896–906. https://doi.org/10.1016/j.ijhydene.2019.08.256.

[5] Panagi K, Laycock CJ, Reed JP, Guwy AJ. Highly efficient coproduction of electrical power and synthesis gas from biohythane using solid oxide fuel cell technology. Appl Energy 2019;255:113854. https://doi.org/10.1016/j.apenergy.2019.113854.

[6] Sarruf BJM, Hong JE, Steinberger-Wilckens R, de Miranda PEV. Ceria-Co-Cu-based SOFC anode for direct utilisation of methane or ethanol as fuels. Int J Hydrogen Energy 2020;45:5297–308. https://doi.org/10.1016/j.ijhydene.2019.04.075.

[7] Tao Z, Hou G, Xu N, Zhang Q. A highly coking-resistant solid oxide fuel cell with a nickel doped ceria: Ce1-xNixO2-y reformation layer. Int J Hydrogen Energy 2014;39:5113–20. https://doi.org/10.1016/j.ijhydene.2014.01.092.

[8] Farrell B, Linic S. Direct electrochemical oxidation of ethanol on SOFCs: Improved carbon tolerance of Ni anode by alloying. Appl Catal B Environ 2016;183:386–93.

https://doi.org/10.1016/j.apcatb.2015.11.002.

[9] Kishimoto H, Yamaji K, Horita T, Xiong Y, Sakai N, Brito ME, et al. Feasibility of liquid hydrocarbon fuels for SOFC with Ni-ScSZ anode. J Power Sources 2007;172:67–71. https://doi.org/10.1016/j.jpowsour.2007.04.042.

[10] Jiang Z, Liao M, Qi J, Wang C, Chen Y, Luo X, et al. Enhancing hydrogen production from propane partial oxidation via CO preferential oxidation and CO2 sorption towards solid oxide fuel cell (SOFC) applications. Renew Energy 2020;156:303–13. https://doi.org/10.1016/j.renene.2020.03.161.

[11] Zhang Y, Yu F, Wang X, Zhou Q, Liu J, Liu M. Direct operation of Ag-based anode solid oxide fuel cells on propane. J Power Sources 2017;366:56–64. https://doi.org/10.1016/j.jpowsour.2017.08.111.

[12] Mehran MT, Park SW, Kim J, Hong JE, Lee SB, Park SJ, et al. Performance characteristics of a robust and compact propane-fueled 150 W-class SOFC power-generation system. Int J Hydrogen Energy 2019;44:6160–71. https://doi.org/10.1016/j.ijhydene.2019.01.076.

[13] Cinti G, Discepoli G, Sisani E, Desideri U. SOFC operating with ammonia: Stack test and system analysis 2016. https://doi.org/10.1016/j.ijhydene.2016.06.070.

[14] Hagen A, Langnickel H, Sun X. Operation of solid oxide fuel cells with alternative hydrogen carriers. Int J Hydrogen Energy 2019;44:18382–92. https://doi.org/10.1016/j.ijhydene.2019.05.065.

[15] Niu B, Jin F, Liu J, Zhang Y, Jiang P, Feng T, et al. Highly carbon– and sulfur–tolerant Sr2TiMoO6−δ double perovskite anode for solid oxide fuel cells. Int J Hydrogen Energy 2019;44:20404–15. https://doi.org/10.1016/j.ijhydene.2019.06.023.

[16] Wang J, Yan D, Pu J, Chi B, Jian L. Fabrication and performance evaluation of planar solid oxide fuel cell with large active reaction area. Int J Hydrogen Energy

2011;36:7234–9. https://doi.org/10.1016/j.ijhydene.2011.03.011.

[17] Sarruf BJM, Hong J-E, Steinberger-Wilckens R, de Miranda PE V. CeO2Co3O4CuO anode for direct utilisation of methane or ethanol in solid oxide fuel cells. Int J Hydrogen Energy 2018;43:6340–51. https://doi.org/https://doi.org/10.1016/j.ijhydene.2018.01.192.

[18] Kan H, Lee H. Sn-doped Ni/YSZ anode catalysts with enhanced carbon deposition resistance for an intermediate temperature SOFC. Appl Catal B Environ 2010;97:108–14. https://doi.org/10.1016/j.apcatb.2010.03.029.

[19] You H, Gao H, Chen G, Abudula A, Ding X. The conversion among reactions at Ni-based anodes in solid oxide fuel cells with low concentrations of dry methane. J Power Sources 2011;196:2779–84. https://doi.org/10.1016/j.jpowsour.2010.09.082.

[20] Cai G, Liu R, Zhao C, Li J, Wang S, Wen T. Anode performance of Mn-doped ceria-ScSZ for solid oxide fuel cell. J Solid State Electrochem 2011;15:147–52. https://doi.org/10.1007/s10008-010-1079-8.

[21] Paradis H, Andersson M, Yuan J, Sundén B. Simulation of alternative fuels for potential utilization in solid oxide fuel cells. Int J Energy Res 2011;35:1107–17. https://doi.org/10.1002/er.1862.

[22] Troskialina L, Steinberger-Wilckens R. The effects of Sn infiltration on dry reforming of biogas at solid oxide fuel cell operating conditions over Ni-YSZ catalysts. IOP Conf Ser Mater Sci Eng 2019;509. https://doi.org/10.1088/1757-899X/509/1/012064.

[23] Wheeldon I, Caners C, Karan K, Peppley B. Utilization of biogas generated from Ontario wastewater treatment plants in solid oxide fuel cell systems: A process modeling study. Int J Green Energy 2007;4:221–31. https://doi.org/10.1080/15435070601015585.

[24] Jiang Z, Arifin NA, Mardle P, Steinberger-Wilckens R. Electrochemical Performance

and Carbon Resistance Comparison between Tin, Copper and Silver-Doped Nickel/Yttria-Stabilized Zirconia Anodes SOFCs Operated with Biogas. J Electrochem Soc 2019;166:F393–8. https://doi.org/10.1149/2.1011906jes.

[25] Chouhan K, Sinha S, Kumar S, Kumar S. Utilization of biogas from different substrates for SOFC feed via steam reforming: Thermodynamic and exergy analyses. J Environ Chem Eng 2019;7. https://doi.org/10.1016/j.jece.2019.103018.

[26] Bochentyn B, Chlipała M, Gazda M, Wang SF, Jasiński P. Copper and cobalt co-doped ceria as an anode catalyst for DIR-SOFCs fueled by biogas. Solid State Ionics 2019;330:47–53. https://doi.org/10.1016/j.ssi.2018.12.007.

[27] Troskialina L, Dhir A, Steinberger-Wilckens R. Improved Performance and Durability of Anode Supported SOFC Operating on Biogas. ECS Tran 2015;68:2503–13.

[28] Cassidy M, Ouweltjes JP, Dekker N. Going Beyond Hydrogen: Non-hydrogen Fuels, Re-oxidation and Impurity Effects on Solid Oxide Fuel Cell Anodes. In: Steinberger-Wilckens R, Lehnert W, editors. Innov. Fuel Cell Technol., The Royal Society of Chemistry; 2011, p. P001-350. https://doi.org/10.1039/9781849732109.

[29] Arifin NA, Steinberger-Wilckens R, Shamsuddin AH. Biogas as alternative SOFC fuel : Research and implementation. IOP Conf Ser Earth Environ Sci 2020;476:012088. https://doi.org/10.1088/1755-1315/476/1/012088.

[30] Kayfeci M, Keçebaş A, Bayat M. Hydrogen production. Sol. Hydrog. Prod. Process. Syst. Technol., Elsevier; 2019, p. 45–83. https://doi.org/10.1016/B978-0-12-814853-2.00003-5.

[31] Dagdougui H, Sacile R, Bersani C, Ouammi A. Hydrogen Production and Current Technologies. Hydrog. Infrastruct. Energy Appl., Elsevier; 2018, p. 7–21. https://doi.org/10.1016/b978-0-12-812036-1.00002-0.

[32] Lackey J, Champagne P, Peppley B. Use of wastewater treatment plant biogas for the

operation of Solid Oxide Fuel Cells (SOFCs). J Environ Manage 2017;203:753–9. https://doi.org/10.1016/j.jenvman.2016.09.006.

[33] Gandiglio M, Lanzini A, Santarelli M, Acri M, Hakala T, Rautanen M. Results from an industrial size biogas-fed SOFC plant (the DEMOSOFC project). Int J Hydrogen Energy 2019. https://doi.org/https://doi.org/10.1016/j.ijhydene.2019.08.022.

[34] Kumaran P, Hephzibah D, Sivasankari R, Saifuddin N, Shamsuddin AH. A review on industrial scale anaerobic digestion systems deployment in Malaysia: Opportunities and challenges. Renew Sustain Energy Rev 2016;56:929–40. https://doi.org/10.1016/J.RSER.2015.11.069.

[35] Johnson GB, Hjalmarsson P, Norrman K, Ozkan US, Hagen A. Biogas Catalytic Reforming Studies on Nickel-Based Solid Oxide Fuel Cell Anodes. Fuel Cells 2016;16:219–34. https://doi.org/10.1002/fuce.201500179.

[36] Hagen A, Winiwarter A, Langnickel H, Johnson G. SOFC Operation with Real Biogas. Fuel Cells 2017;17:854–61. https://doi.org/10.1002/fuce.201700031.

[37] Andresen B, Norheim A, Strand J, Ulleberg Ø, Vik A, Wærnhus I. BioZEG – Pilot Plant Demonstration of High Efficiency Carbon Negative Energy Production. Energy Procedia 2014;63:279–85. https://doi.org/10.1016/j.egypro.2014.11.030.

[38] Saadabadi SA, Thallam Thattai A, Fan L, Lindeboom REF, Spanjers H, Aravind P V. Solid Oxide Fuel Cells fuelled with biogas: Potential and constraints. Renew Energy 2019;134:194–214. https://doi.org/10.1016/j.renene.2018.11.028.

[39] Boldrin P, Ruiz-Trejo E, Mermelstein J, Bermúdez JM, Ramirez Reina T, Brandon N. Strategies for Carbon and Sulfur Tolerant Solid Oxide Fuel Cell Materials, Incorporating Lessons from Heterogeneous Catalysis. Chem Rev 2016;116. https://doi.org/10.1021/acs.chemrev.6b00284.

[40] Sumi H, Puengjinda P, Muroyama H, Matsui T, Eguchi K. Effects of crystal Structure

641 of yttria- and scandia-stabilized zirconia in nickel-based SOFC anodes on carbon
642 deposition and oxidation behavior. J Power Sources 2011;196:6048–54.
643 https://doi.org/10.1016/j.jpowsour.2011.03.092.
644 [41] Sumi H, Lee YH, Muroyama H, Matsui T, Kamijo M, Mimuro S, et al. Effect of
645 carbon deposition by carbon monoxide disproportionation on electrochemical
646 characteristics at low temperature operation for solid oxide fuel cells. J Power Sources
647 2011;196:4451–7. https://doi.org/10.1016/j.jpowsour.2011.01.061.
648 [42] Singh A, Hill JM. Carbon tolerance, electrochemical performance and stability of solid
649 oxide fuel cells with Ni/yttria stabilized zirconia anodes impregnated with Sn and
650 operated with methane. J Power Sources 2012;214:185–94.
651 https://doi.org/10.1016/j.jpowsour.2012.04.062.
652 [43] Sumi H, Ukai K, Mizutani Y, Mori H, Wen C-J, Takahashi H, et al. Performance of
653 nickel–scandia-stabilized zirconia cermet anodes for SOFCs in 3% H 2O–CH 4. Solid
654 State Ionics 2004;174:151–6. https://doi.org/10.1016/j.ssi.2004.06.016.
655 [44] Sayas S, Vivó N, Da Costa-Serra JF, Chica A. Toluene steam reforming over nickel
656 based catalysts. Int J Hydrogen Energy 2020.
657 https://doi.org/10.1016/j.ijhydene.2020.04.235.
658 [45] Wei Q, Gao X, Wang L, Ma Q. Rational design of nickel-based catalyst coupling with
659 combined methane reforming to steadily produce syngas. Fuel 2020;271:117631.
660 https://doi.org/10.1016/j.fuel.2020.117631.
661 [46] Fedorova ZA, Danilova MM, Zaikovskii VI. Porous nickel-based catalysts for tri-
662 reforming of methane to synthesis gas: Catalytic activity. Mater Lett 2020;261:127087.
663 https://doi.org/10.1016/j.matlet.2019.127087.
664 [47] Majewski AJ, Wood J. Tri-reforming of methane over Ni@SiO2 catalyst. Int J
665 Hydrogen Energy 2014;39:12578–85. https://doi.org/10.1016/j.ijhydene.2014.06.071.

[48] Sazali N. Emerging technologies by hydrogen: A review. Int J Hydrogen Energy 2020. https://doi.org/10.1016/j.ijhydene.2020.05.021.

[49] Gorte RJ, Vohs JM, McIntosh S. Recent developments on anodes for direct fuel utilization in SOFC. Solid State Ionics 2004;175:1–6. https://doi.org/10.1016/j.ssi.2004.09.036.

[50] Bian L, Wang L, Duan C, Cai C, Song X, An S. Co-free La0.6Sr0.4Fe0.9Nb0.1O3-δ symmetric electrode for hydrogen and carbon monoxide solid oxide fuel cell. Int J Hydrogen Energy 2019;44:32210–8. https://doi.org/10.1016/j.ijhydene.2019.10.090.

[51] Shu L, Sunarso J, Hashim SS, Mao J, Zhou W, Liang F. Advanced perovskite anodes for solid oxide fuel cells: A review. Int J Hydrogen Energy 2019;44:31275–304. https://doi.org/10.1016/j.ijhydene.2019.09.220.

[52] Futamura S, Muramoto A, Tachikawa Y, Matsuda J, Lyth SM, Shiratori Y, et al. SOFC anodes impregnated with noble metal catalyst nanoparticles for high fuel utilization. Int J Hydrogen Energy 2019;44:8502–18. https://doi.org/https://doi.org/10.1016/j.ijhydene.2019.01.223.

[53] Arifin NA, Button TW, Steinberger-Wilckens R. Carbon-tolerant Ni/ScCeSz via aqueous tape casting for IT-SOFCs. ECS Trans 2017;78:1417–25. https://doi.org/10.1149/07801.1417ecst.

[54] Ke K, Gunji a., Mori H, Tsuchida S, Takahashi H, Ukai K, et al. Effect of oxide on carbon deposition behavior of CH4 fuel on Ni/ScSZ cermet anode in high temperature SOFCs. Solid State Ionics 2006;177:541–7. https://doi.org/10.1016/j.ssi.2005.12.009.

[55] Eguchi K, Tanaka K, Matsui T, Kikuchi R. Reforming activity and carbon deposition on cermet catalysts for fuel electrodes of solid oxide fuel cells. Catal Today 2009;146:154–9. https://doi.org/10.1016/j.cattod.2009.01.033.

[56] Takeguchi T, Kikuchi R, Yano T, Eguchi K, Murata K. Effect of precious metal

addition to Ni-YSZ cermet on reforming of CH4 and electrochemical activity as SOFC anode. Catal Today 2003;84:217–22. https://doi.org/10.1016/S0920-5861(03)00278-5.

[57] Niakolas DK, Ouweltjes JP, Rietveld G, Dracopoulos V, Neophytides SG. Au-doped Ni/GDC as a new anode for SOFCs operating under rich CH4 internal steam reforming. Int J Hydrogen Energy 2010;35:7898–904. https://doi.org/https://doi.org/10.1016/j.ijhydene.2010.05.038.

[58] Nikolla E, Schwank J, Linic S. Promotion of the Long-Term Stability of Reforming Ni Catalysts by Surface Alloying. J Catal - J CATAL 2007;250:85–93. https://doi.org/10.1016/j.jcat.2007.04.020.

[59] Anwar M, Muhammed Ali SA, Abdalla AM, Somalu MR, Muchtar A. Effect of sintering temperature on the microstructure and ionic conductivity of Ce0.8Sm0.1Ba0.1O2-δ electrolyte. Process Appl Ceram 2017;11:67–74. https://doi.org/10.2298/PAC1701067A.

[60] Jiang Z, Arifin NA, Mardle P, Steinberger-Wilckens R. Electrochemical Performance and Carbon Resistance Comparison between Tin, Copper and Silver-Doped Nickel/Yttria-Stabilized Zirconia Anodes SOFCs Operated with Biogas. J Electrochem Soc 2019;166:F393–8. https://doi.org/10.1149/2.1011906jes.

[61] Lay E, Metcalfe C, Kesler O. Influence of Tertiary Phases Incorporated into Ni-based Cermets by Solution Precursor Plasma Spraying (SPSS) on Anode Stability. ECS Trans 2011;35:1303–13. https://doi.org/10.7868/s0869565214210269.

[62] Wang C, Luo L, Wu Y, Hou B, Sun L. A novel multilayer aqueous tape casting method for anode-supported planar solid oxide fuel cell. Mater Lett 2011;65:2251–3. https://doi.org/10.1016/j.matlet.2011.04.077.

[63] Schafbauer W, Menzler NH, Buchkremer HP. Tape casting of anode supports for solid oxide fuel cells at Forschungszentrum Julich. Int J Appl Ceram Technol 2014;11:125–

716 35. https://doi.org/10.1111/j.1744-7402.2012.02839.x.
717 [64] Stambouli AB, Traversa E. Solid oxide fuel cells (SOFCs): A review of an
718 environmentally clean and efficient source of energy. Renew Sustain Energy Rev
719 2002;6:433–55. https://doi.org/10.1016/S1364-0321(02)00014-X.
720 [65] Taroco H, Santos J, Domingues R, Matencio T. Ceramic Materials for Solid Oxide
721 Fuel Cells, 2011.
722 [66] Huang K, Goodenough JB. Performance characterization techniques for a solid oxide
723 fuel cell (SOFC) and its components. Solid Oxide Fuel Cells Technol., Woodhead
724 Publishing; 2009, p. 156–82.
725 https://doi.org/https://doi.org/10.1533/9781845696511.156.
726 [67] Baker RTK. Catalytic growth of carbon filaments. Carbon N Y 1989;27:315–23.
727 https://doi.org/https://doi.org/10.1016/0008-6223(89)90062-6.
728 [68] Mallon C, Kendall K. Sensitivity of nickel cermet anodes to reduction conditions. J
729 Power Sources 2005;145:154–60.
730 https://doi.org/https://doi.org/10.1016/j.jpowsour.2005.02.043.
731 [69] Dhir A, Kendall K. Microtubular SOFC anode optimisation for direct use on methane.
732 J Power Sources 2008;181:297–303.
733 https://doi.org/https://doi.org/10.1016/j.jpowsour.2007.11.005.
734 [70] Somalu MR, Yufit V, Cumming D, Lorente E, Brandon NP. Fabrication and
735 characterization of Ni/ScSZ cermet anodes for IT-SOFCs. Int J Hydrogen Energy
736 2011;36:5557–66. https://doi.org/10.1016/j.ijhydene.2011.01.151.
737 [71] Troskialina L. Improved Performance of Solid Oxide Fuel Cell Operating on Biogas
738 using Tin Anode-infiltration (Ph.D. Thesis). University of Birmingham, 2016.
739 https://doi.org/http://etheses.bham.ac.uk/id/eprint/6790.
740 [72] Arifin NA. Developing carbon tolerant Ni/ScCeSZ cells via aqueous tape casting for

direct biogas fed solid oxide fuel cells (SOFC) Ph.D. Thesis. University of Birmingham, 2019.